


Article

Experimental and Numerical Study of an Active Solar Heating System with Soil Heat Storage for Greenhouses in Cold Climate Zones

Tao Yu ¹, Dongju Wang ², Xintian Zhao ¹, Jiyong Liu ^{1,3,*}  and Moon Keun Kim ⁴

¹ Thermal Engineering Department, Shandong Jianzhu University, Jinan 250101, China; yutao1978@sdjzu.edu.cn (T.Y.); xt_zhao98@163.com (X.Z.)

² Jintian Industrial Development (Shandong) Group Co., Ltd., Jinan 250014, China; hgdyutao@sina.com

³ Shandong GRAD Group, Built Environment Design and Research Institute, Dezhou 253000, China

⁴ Department of Civil Engineering and Energy Technology, Oslo Metropolitan University, N-0130 Oslo, Norway; moonkeun@oslomet.no

* Correspondence: jxl83@sdjzu.edu.cn

Abstract: Root temperature is an important ecological factor affecting plant growth. A solar greenhouse with an active solar heating system was built in Jinan, in the cold climate zone of northern China. Experiments encompassing the complete cycle of heat collection, heat storage, and heat release were carried out. Using the experimental data, the numerical simulation of soil heat storage with a variable heat flow was executed using the ANSYS (ANSYS Inc., Pittsburgh, PA, USA) Fluent software. Soil temperature fields were studied on typical sunny days and typical cloudy days in the transition season and winter. The solar collector efficiency and coefficient of performance of the system were investigated. The applicability of this active solar soil heating system with soil heat storage for cold areas was evaluated. The results showed that the system effectively maintained suitable ground temperatures to prevent plant growth inhibition caused by low ground temperatures in winter. During the experimental period, the solar collector efficiency was 47% and the system's coefficient of performance was 67.70. The thermal performance of the system was much better than a traditional energy system. This study showed that this active solar heating system with soil heat storage is an economic and feasible way to increase soil temperatures in solar greenhouses in cold areas.

Keywords: greenhouse; active solar heating system; soil heat storage; soil temperature; experiment



Citation: Yu, T.; Wang, D.; Zhao, X.; Liu, J.; Kim, M.K. Experimental and Numerical Study of an Active Solar Heating System with Soil Heat Storage for Greenhouses in Cold Climate Zones. *Buildings* **2022**, *12*, 405. <https://doi.org/10.3390/buildings12040405>

Academic Editor: Francesco Asdrubali

Received: 8 February 2022

Accepted: 18 March 2022

Published: 26 March 2022

Publisher's Note: MDPI stays neutral with regard to jurisdictional claims in published maps and institutional affiliations.



Copyright: © 2022 by the authors. Licensee MDPI, Basel, Switzerland. This article is an open access article distributed under the terms and conditions of the Creative Commons Attribution (CC BY) license (<https://creativecommons.org/licenses/by/4.0/>).

1. Introduction

In the Northern Hemisphere, solar greenhouses are constructed with north-facing back walls and south-facing transparent covers, and are regarded as important agricultural facilities that enrich vegetable growth and increase farmers' incomes in cold climate zones [1,2]. Traditional solar greenhouses mainly use the back wall to store energy from the solar radiation collected during the day, to release it during the night. Due to their low running costs and energy saving potential, solar greenhouses have increasingly gained popularity and are widely used in the northern villages of China [3].

Although solar greenhouses can provide suitable environmental conditions for the intensive production of various crops, they are mostly used in spring and autumn; crops cannot grow well in winter because of the low air temperature inside the green house and low soil temperature. The soil temperature around the roots of crops is an important ecological factor determining crop growth [4]. Low soil temperatures in root zones not only directly affect the absorption functions, transportation functions, and hormone metabolism of roots, but also photosynthesis and respiration of plants, resulting in slow crop growth and low yields [5]. Therefore, to improve crop growth, it is important to maintain suitable

soil temperatures in greenhouses, especially when ambient temperatures are low. In order to avoid the consumption of conventional energy sources and reduce greenhouse gas emissions, it is preferable to use renewable energies such as solar energy, which has demonstrated great potential for integration into agricultural greenhouses [6].

The literature contains numerous reports where a variety of measures have been taken to increase soil temperature using renewable energies [7]. Kurpaska and Slipek [8] designed two greenhouse substratum heating systems: buried pipes and vegetation heating. Their analysis showed that, for similar substrate temperature conditions, the vegetation heating system required water temperatures 3 K higher than the buried pipe system, and heat loss was higher in the vegetation system. Bernier et al. [9] built a soil heat exchanger-storage system in a greenhouse made of 26 non-perforated, 102 mm corrugated plastic drainage pipes buried in the soil of a conventional greenhouse, which were 12 m long, and 450 mm and 750 mm deep. Their experiment showed that the average coefficient of performance of the system during the test was 4.6, demonstrating that this system reduced the energy demand of the greenhouse. Attar et al. [10] proposed a solar water heating system for greenhouse heating in Tunisia which used capillary heat exchangers integrated into the greenhouse and which stored heat in the ground. The cost and efficiency of the system were estimated for different greenhouses sizes, and it was concluded that the heating cost of a 1000 m³ greenhouse was reduced by 51.8% in April, and that the system would be sufficient to heat a 10 m³ greenhouse. Zhang et al. [11] invented a seasonal solar soil heat storage system composed of solar collectors and U-pipe heat exchangers, and used TRNSYS (Thermal Energy System Specialists, LLC, Madison, USA) to simulate the process and effect of solar energy collection and soil heat storage. Their results showed that, in Shanghai, when the indoor air temperature of the greenhouse was kept above 12 °C throughout the year, the annual energy savings was 27.8 kWh/m².

Khalid et al. [12] introduced a greenhouse that integrated roof-mounted solar air heaters into a conventional greenhouse. They examined performance on clear and partly cloudy winter days by developing a dynamic model, including the soil surface heat exchange with the greenhouse air, and indicated that buried storage inside the greenhouse soil was much more beneficial than heat storage outside the greenhouse. Awani et al. [13] studied the performance of a heat pump system assisted by solar and geothermal energy under the climatic conditions of Tunisia. They showed that a horizontal heat exchanger can effectively heat greenhouses, evidenced by the fact that reductions in ground temperature did not exceed 1 °C. The solar and geothermal-energy-assisted heat pump in heating mode saved on conventional energy and was comparable to traditional heating systems. Attar et al. [14] presented a TRNSYS simulation to evaluate the performances of a solar water heating system used for greenhouses exposed to the Tunisian weather. They investigated all possible combinations of two solar collectors, while also manipulating the inlet flow rate, tank volume, and collector area. Their simulation showed that, by increasing the tank volume, the temperature at the collector outlet was decreased. In addition, a high flow rate minimized stratification and increased the efficiency of the system. Gauthier et al. [15] presented a transient, fully three-dimensional heat transfer model based on the coupled conservation equations of energy in the soil and the circulated air. The model was used to examine the effects of various design and operating parameters on system performance. Their results indicated that burying pipes deeper underground allowed more energy to be stored during the day, but less was recovered to the ground surface at night and the overall performance declined.

Through reviewing existing studies, it was clear that soil heat storage technologies utilizing solar radiation are efficient energy-saving measures that can prevent damage to crops in the extreme cold of winter, even over consecutive overcast days. However, there have been few experimental studies conducted focusing on the influence of soil temperature variability when utilizing solar heating systems. Therefore, to study the effect of soil temperature on soil heat storage in winter in northern China, this study constructed an active solar heating system with soil heat storage for a plastic greenhouse located

in Jinan city, and comprehensively monitored the experiment, including heat collection, heat storage, and heat release from 23 September 2019 to 8 March 2020. Moreover, this study built a three-dimensional geometric model of the horizontal heating pipes and soil to numerically simulate the soil heat storage and release process during the transitional season and sunny and cloudy days in winter. Finally, the applicability of the soil heat storage system in a cold climate zone was evaluated by considering soil temperature, heat collection efficiency, and system energy efficiency, to provide a reference for the selection of soil heating methods for solar greenhouses.

2. Method

2.1. Solar Greenhouse Description

As shown in Figure 1, the experimental greenhouse faced south, had a ridge height of 5 m, and was 70 m long from east to west, and 11 m deep along the north–south axis. The rear wall was composed of a 370 mm brick outer wall and a 120 mm brick inner wall. A 50 mm polystyrene insulation layer was set outside the outer wall. The structures of the east and west gable walls were the same as those of the back wall. The gable walls were built following the shape of an arch frame. The front roof was composed of a 240 mm reinforced concrete girt and a $\Phi 59 \times 2$ hot-dip galvanized steel pipe arch beam. This was covered with ethylene vinyl acetate copolymer (EVA) film, which has good thermal insulation and light transmittance characteristics. The greenhouse was equipped with a cotton blanket insulation layer whose extension and retraction were electrically controlled. The thermal parameters of the enclosure are shown in Table 1.

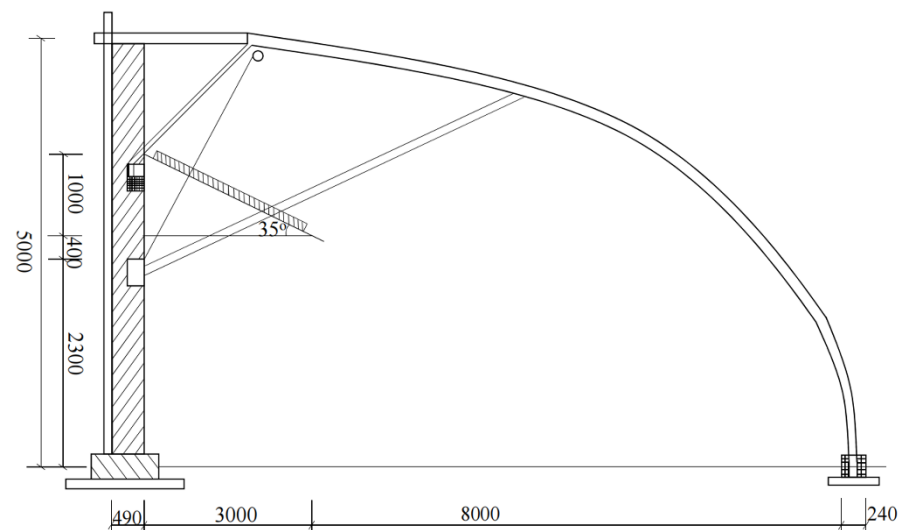


Figure 1. Sectional drawing of the typical solar greenhouse design (lengths in mm).

Table 1. Thermal parameters of the enclosure structure.

Item	Structure	Thermal Conductivity W/(m·K)	Density kg/m ³	Specific Heat Capacity J/(kg·°C)	Area m ²	U-Value W/(m ² ·K)
Walls (north, east, west)	20 mm cement sand plaster	0.93	1800	1050	427.96	0.49
	50 mm polystyrene board	0.042	30	1380		
	370 mm brick wall	0.79	1500	1070		
	120 mm brick wall	0.79	1500	1070		
	20 mm cement sand plaster	0.93	1800	1050		
Film	0.16 mm EVA	0.047	20	1465	788.47	6.18

2.2. Active Solar Heating System with Soil Heat Storage

The active solar heating system of the experimental greenhouse is shown in Figure 2. After being heated by absorbed solar energy, the water in the collector fluid channels enters

the water storage tank. Driven by the water pump, the hot water flows into buried plastic heating pipes via the water separator to release heat to the soil. After heat transfer to the soil, the water is collected and returned to the water storage tank.

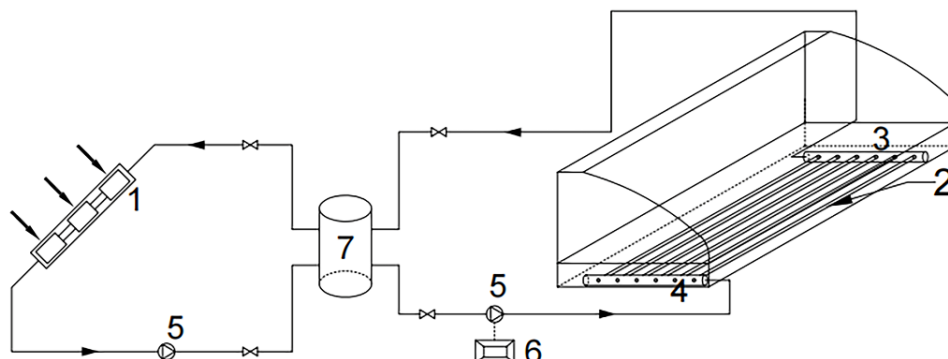


Figure 2. Schematic diagram of solar soil heating system. (1. solar collector, 2. horizontal heating pipes, 3. water collector, 4. water separator, 5. water pump, 6. controlling cabinet, 7. water storage tank.).

The solar collector is a flat plate collector, model P-B/0.2-U/GL-1.86-1, produced by Sanqi New Energy Company, Jinan, China. The plate core of the solar collector was designed with a full flow channel. The solar collector absorber coating was composed of six nanolayers and coated by PVD (Physical Vapor Deposition) magnetron sputtering technology. The cover plate was high-permeability tempered glass. The experimental system was equipped with 45 flat plate solar collectors, with single plate areas of 2 m² (effective heat collection area of 1.86 m²) and a total effective heat collection area of 83.7 m². Every five collectors were connected in series as a group, and the groups were connected in parallel. Due to the limited external installation space, and in order to avoid blocking sunlight projected onto adjacent greenhouses, the heat collector was installed within the greenhouse in a built-in manner.

The solar collector was fixed on the rear wall using a bracket, and the lower end of the bracket was fixed to the foundation beam using expansion bolts. The collector was installed at a 28° angle (Figure 3).

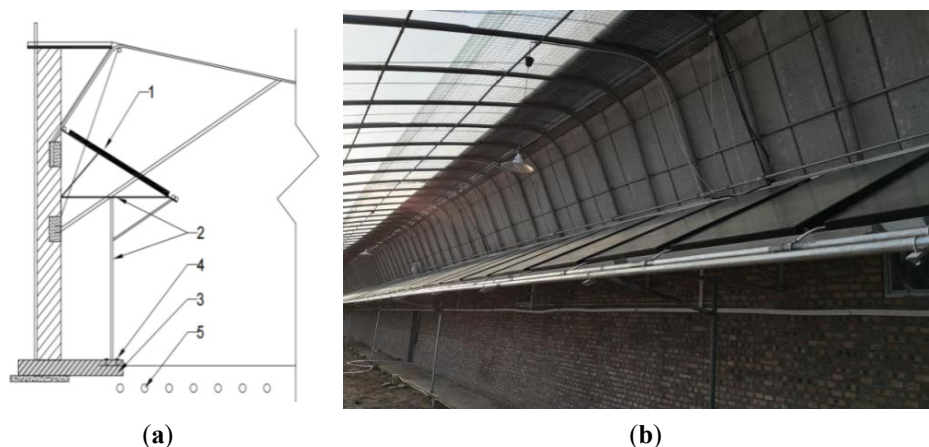


Figure 3. Installation of the solar collector. (a) Sectional view of the solar collector and (b) on-site installation of the solar collector. (1. solar collector, 2. support structure, 3. ground beam, 4. expansion bolt, 5. buried pipes.).

The buried heating pipes were PE-RT (polyethylene of raised temperature resistance) pipes with an outer diameter of 25 mm and a wall thickness of 2.5 mm. The underground pipes were spaced 20 cm apart and each pipe was 65 m long. The heating pipes were

laid horizontally and straight as shown in Figure 4. Tomato plants were planted in the greenhouse. Tomato root systems are mainly distributed in the cultivated layer at depths of 0–60 cm, and the taproot depth at the seedling stage can reach 40–50 cm [16]. Therefore, in order not to affect crop root growth, the buried depth of heating tubes was set to 0.7 m.



Figure 4. Horizontal heating pipe layout.

The polypropylene heat storage tank had a volume of 5 m^3 , a wall thickness of 0.008 m, a bottom diameter of 1.78 m, and a total height of 2.3 m (Figure 5). It was buried in the soil. The circulating water pump was model PW-251EH, with a flow rate of $1.68 \text{ m}^3/\text{h}$, a head of 20 m, and a pump power of 500 W.

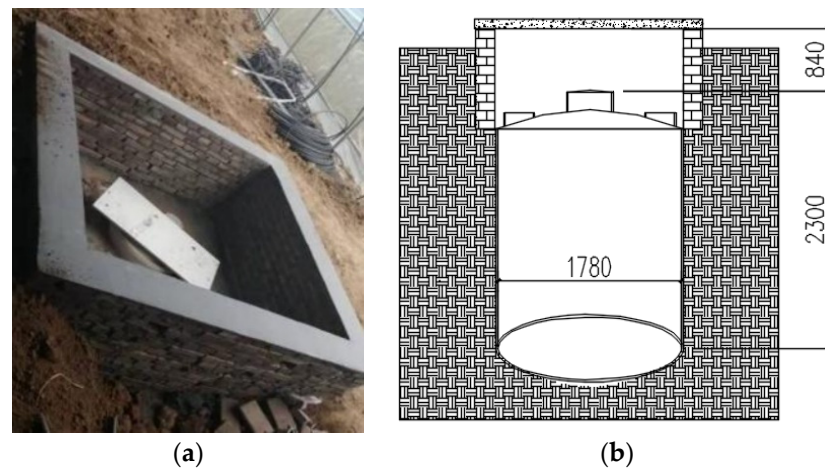


Figure 5. Structure of the buried water tank. (a) Water tank installation site and (b) Schematic diagram of tank size.

To maximize the extraction of heat energy from the collector, the pump was started and stopped according to the difference in temperature between the collector water temperature and the soil temperature at a depth of 15 cm. When the temperature difference was greater than or equal to $7 \text{ }^\circ\text{C}$, the circulating water pump was turned on, and the hot water was circulated through the horizontal heating pipes in the soil for heat exchange. When the temperature difference was less than or equal to $3 \text{ }^\circ\text{C}$, the circulating water pump was closed, and heat exchange was halted. The control strategy of the system is shown in Figure 6, wherein T_{-15} is the soil temperature at a depth of 15 cm and T_{out_c} is the water temperature at the collector outlet.

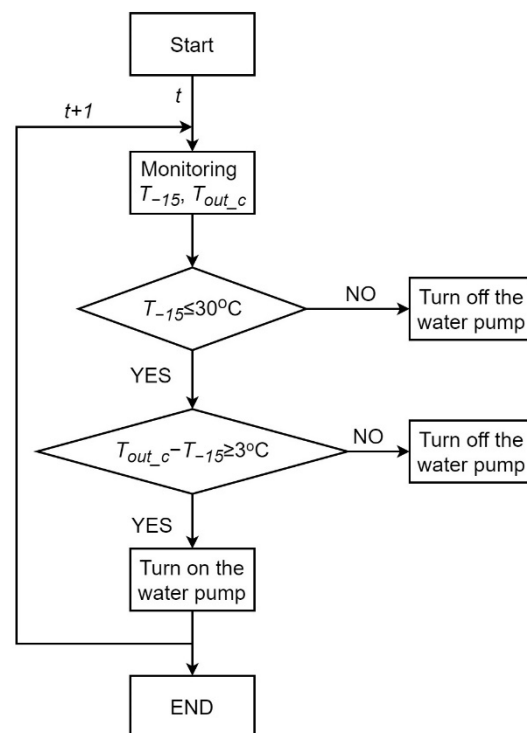


Figure 6. Schematic diagram of the water pump control strategy.

2.3. Experiment

2.3.1. Field Study

The experimental greenhouse was located in Jinan City, Shandong Province, China (36.7° N, 117° E), with an annual average temperature of 14.7 °C (Figure 7). Jinan belongs to the cold climate zone of China's dividing region, and its average temperature in the coldest month is −1.4 °C. The extreme low temperature in Jinan during the study period was −12.1 °C. From November 22 to March 3 of the following year (a total of 99 days), which is the greenhouse heating season, the daily average temperature was below 5 °C. Jinan is rich in solar energy resources. There are 4252 annual sunshine hours; the average total solar radiation intensity is about 330 W/m²; the maximum hourly total radiation intensity is 1051 W/m²; the annual total radiation intensity is 1.4 MWh/m² [17]. The hourly outdoor temperature and solar radiation intensity in Jinan during the experimental period are shown in Figure 8.

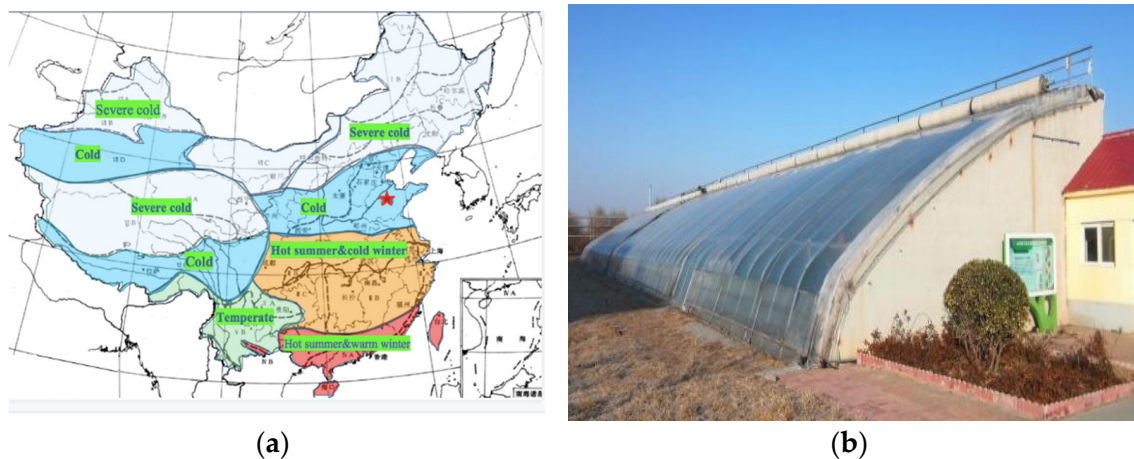


Figure 7. The climate location of Jinan and an external photograph of the solar greenhouse. (a) The climate location of Jinan city and (b) The external photograph of the solar greenhouse.

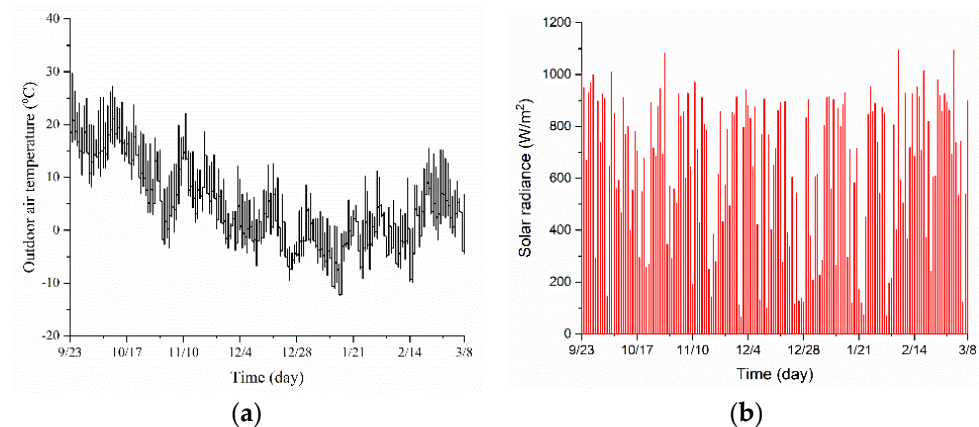


Figure 8. Weather conditions in Jinan during the experiment. (a) Outdoor air temperature and (b) Solar radiation.

2.3.2. Experimental Parameters and Instruments

To monitor the operating parameters of the system, the measuring points shown in Figure 9 were arranged in advance of the construction stage. At points 1 and 2, two temperature sensors were set to measure the outlet and inlet water temperatures of the collector, respectively. Two soil temperature sensors were set at point 3 to measure the soil temperature at 15 cm and 30 cm underground. The indoor environmental monitoring station was set at point 4 to monitor illumination, air temperature, and moisture in the greenhouse. A temperature sensor was set at point 5 to monitor the outlet water temperature of the water storage tank. The illumination, air temperature, and moisture were displayed in real time on a display screen on the west wall of the greenhouse, and data were transmitted wirelessly and recorded at 20-min intervals by the mainframe computer. The intelligent control box collected parameters, such as the outlet and inlet water temperatures of the collector, the outlet water temperature of the water storage tank, and the soil temperature every minute. As shown in Figure 10, each start and stop of the circulating pump was recorded as a digital output, and all data were stored on a data cloud platform. The characteristics of the experimental instrument are shown in Table 2.

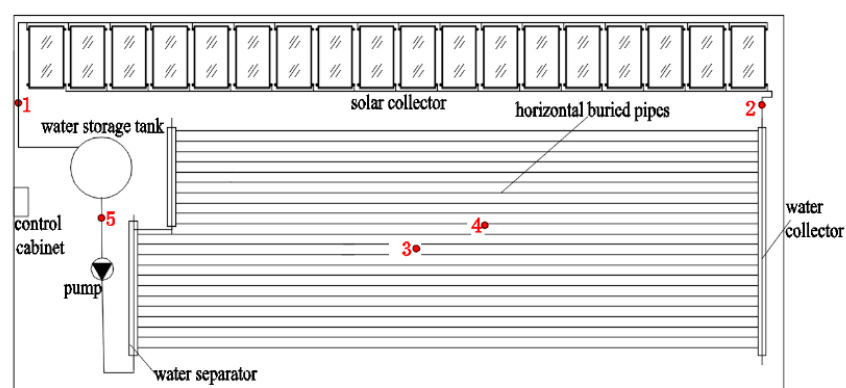


Figure 9. Schematic diagram of measuring point locations. (1. outlet water temperature of collector, 2. inlet water temperature of collector, 3. soil temperature at 15 cm and 30 cm depths, 4. indoor environmental parameters, 5. outlet temperature of water storage tank.).



Figure 10. The cloud platform for the field experimental system.

Table 2. Summary of the experimental instruments.

Item	Model	Range	Accuracy
Temperature sensor	NTC thermistor	−20–100 °C	±1 °C
Soil moisture and temperature sensor	RS-ECTH-N01	Soil temperature: −40–80 °C Soil humidity: 0–100%	Soil temperature: ±0.5 °C Soil humidity: ±2% (0–50%), ±3% (50–100%)
Indoor environmental monitoring station	NXT-A6	Air temperature: −40–125 °C Air humidity: 0–100% Illuminance: 0–200 Klx	Air temperature: ±0.2 °C Air humidity: ±3% Illuminance: ±0.06 Klx

2.3.3. Evaluating Indicators

(1) Soil temperature: The optimum temperature for tomato root growth is 20–22 °C. Root growth is slowed when soil temperature is lower than 12 °C. Root hairs stop growing when the soil temperature is lower than 8 °C, and crop taproots stop growing when the soil temperature further drops below 6 °C. Therefore, the minimum soil temperature at each depth should not be lower than 12 °C.

(2) Solar collector efficiency: The solar radiation intensity measured the solar radiation received on the horizontal plane, while the solar collector surface was at an inclined plane. Therefore, it was necessary to convert the solar radiation on the horizontal plane to the inclined plane. So, the total solar radiation intensity, I_{θ} , on the inclined surface is composed of direct radiation intensity, $I_{b,\theta}$, scattered radiation intensity, $I_{d,\theta}$, and ground reflected radiation intensity, $I_{r,\theta}$ (see Equation (1)) [18].

$$I_{\theta} = I_{b,\theta} + I_{d,\theta} + I_{r,\theta} \quad (1)$$

The direct radiation intensity on the inclined surface is calculated by Equation (2):

$$I_{b,\theta} = I_b \cdot \cos \beta / \cos i \quad (2)$$

where I_b is the intensity of direct solar radiation on the horizontal plane, W/m^2 ; β is the solar collector installation angle, and i is the incidence angle.

The scattered radiation intensity on the inclined plane is drawn from Equation (3):

$$I_{d,\theta} = \frac{I_d(1 + \cos \beta)}{2} \quad (3)$$

where I_d is the intensity of solar scattered radiation on horizontal plane, W/m^2 .

The solar radiation intensity reflected from the ground is calculated by Equation (4):

$$I_{r,\theta} = R_g(I_d + I_b)(1 - \cos \beta)/2 \quad (4)$$

where R_g is the ratio of reflected radiation to incident radiation, which is generally taken as 0.2, but when the surface is covered with snow, it is taken as 0.7 [19].

The total solar radiant energy Q_A received by the collector is shown in Equation (5) [20].

$$Q_A = A \cdot I_{\theta}(\tau\alpha)_e \quad (5)$$

where A is the area of solar collector and m^2 ; $(\tau\alpha)_e$ is the product of the transmission ratio of transparent cover plate and absorption ratio of heat absorber. It is calculated according to reference [20,21].

At time τ , the instantaneous effective heat collection of the collector is calculated by Equation (6):

$$Q_{U,\tau} = m_c c_p (T_{out_c,\tau} - T_{in_c,\tau}) \quad (6)$$

where $Q_{U,\tau}$ is the instantaneous effective heat collection of the solar collector at time τ , W; $T_{out_c,\tau}$ is outlet water temperature of the collector at time τ , °C; $T_{in_c,\tau}$ is the inlet water temperature of the solar collector at time τ , °C; m_c is the mass flow of the circulating working medium in the solar collector, kg/s; c_p is the specific heat capacity of the fluid at a constant pressure, J/(kg·°C).

The corresponding solar collector efficiency is shown in Equation (7).

$$\bar{\eta} = 100 \times \frac{\sum_{i=0}^n Q_{U,\tau}(i)}{\sum_{i=0}^n Q_A(i)} \% = 100 \times \frac{\sum_{i=0}^n m_c c_p (T_{out_c,\tau} - T_{in_c,\tau})}{\sum_{i=0}^n A I_{\theta}(i) (\tau\alpha)_e} \% \quad (7)$$

where $\bar{\eta}$ is the average solar collector efficiency during the calculation period, and i is the serial number in a calculation period.

(3) COP: The coefficient of performance (COP) of the system is defined as the ratio of heat released, to soil and energy consumed by the circulation pump within the calculation period, as shown in Equation (8).

$$COP = \frac{\sum_{i=0}^n m_c c_p (T_{out_t,\tau} - T_{in_t,\tau}) \Delta t}{N \cdot t} \quad (8)$$

where $T_{out_t,\tau}$ is outlet temperature of the water storage tank at time τ , °C; Δt is the time interval for data collection, which is 60 s for this experiment; N is pump power, W; t is the operation time of the water pump, s.

2.4. CFD Numerical Simulation

2.4.1. Three-Dimensional Geometrical Model

The heat transfer from heating pipes to soil is an unsteady three-dimensional heat transfer process affected by multiple factors, such as burial depth and distance between heating pipes, fluid temperature and flow regime inside pipes, soil physical parameters, underground water migration, etc. In this paper, the soil outside the pipe was simplified into a cuboid computing domain of 0.8 m × 65.0 m × 1.4 m. Considering the coupled effects of heat transfer between horizontal heating pipes, four horizontal pipes in non-edge zones were taken as the calculation unit to establish a three-dimensional physical model, as shown in Figure 11.

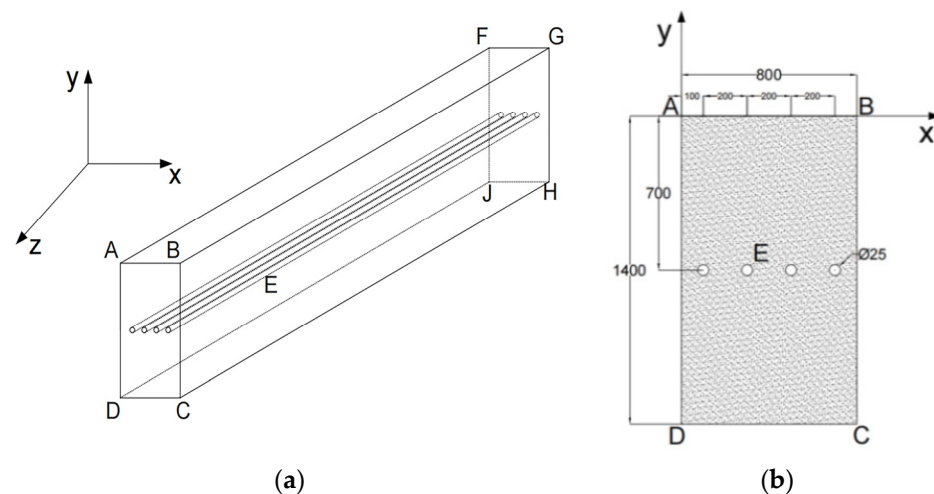


Figure 11. Physical model of horizontal heating pipe and surrounding soil. (a) Isometric view and (b) sectional view.

The following assumptions were made: The fluid in the heating pipe is incompressible and its density is constant. The thermophysical properties of soil are isotropic and constant. Heat and moisture transfer caused by water transfer within soil is negligible. The contact thermal resistance between soil and heating pipe is negligible. The soil at a certain depth has a constant temperature.

2.4.2. Mathematical Model

The fluid flow and heat transfer in the heating pipe follow the laws of energy conservation, mass conservation, and momentum conservation. The governing heat conduction equation between heating pipe and surrounding soil is shown in Equation (9), and the boundary conditions of each wall surface are shown in Equations (10)–(13).

$$\frac{\partial T}{\partial t} = \frac{\lambda_s}{\rho_s c_s} \left(\frac{\partial T^2}{\partial x^2} + \frac{\partial T^2}{\partial y^2} + \frac{\partial T^2}{\partial z^2} \right) \quad (9)$$

$$\tau > 0, 0 \text{ mm} < x \leq 800 \text{ mm}, -1400 \text{ mm} < y \leq 0 \text{ mm}, -65,000 \text{ mm} < z \leq 0 \text{ mm}$$

$$-\lambda_s \frac{\partial T}{\partial x} \Big|_{AB} = \alpha_s I_g + h_c (T_{av,s} - T_a) \quad (10)$$

$$q_w = q_f \quad (11)$$

$$\frac{\partial t}{\partial n} \Big|_{AD,BC} = 0 \quad (12)$$

$$T|_{CD} = T_{c,s} \quad (13)$$

where λ_s is the thermal conductivity of the soil, $W/(m \cdot K)$; ρ_s is the density of the soil, kg/m^3 ; c_s is the heat capacity of the soil, $J/(kg \cdot ^\circ C)$; α_s is the absorptivity of the ground for solar radiation; I_g is the solar radiation projected onto the ground, W/m^2 ; h_c is convective heat transfer coefficient between the soil surface and air, $W/(m^2 \cdot ^\circ C)$; $T_{av,s}$ is the average soil surface temperature, $^\circ C$; T_a is the air temperature in the greenhouse, $^\circ C$; q_w is the heat flux on the side of the horizontal pipe wall, $J/(m^2 \cdot s)$; q_f is the heat flux of fluid, $J/(m^2 \cdot s)$; $T_{c,s}$ is the constant temperature of deep soil, which is set at $12 \text{ }^\circ C$.

2.4.3. Grid Distribution

The calculation domain is divided into a grid to form discrete areas. In view of the regular structure of the physical model of the research object, a structural grid was selected

and the computing domain inside and around the horizontal pipe was divided into an O-type grid. Considering that the intense heat transfer between the fluid and soil occurs at the pipe wall, the grid near the pipe wall was encrypted. Because the heating pipe is sufficiently long for the fluid inside to reach a fully developed state, the grid along the pipe's length is relatively coarse, as shown in Figure 12.

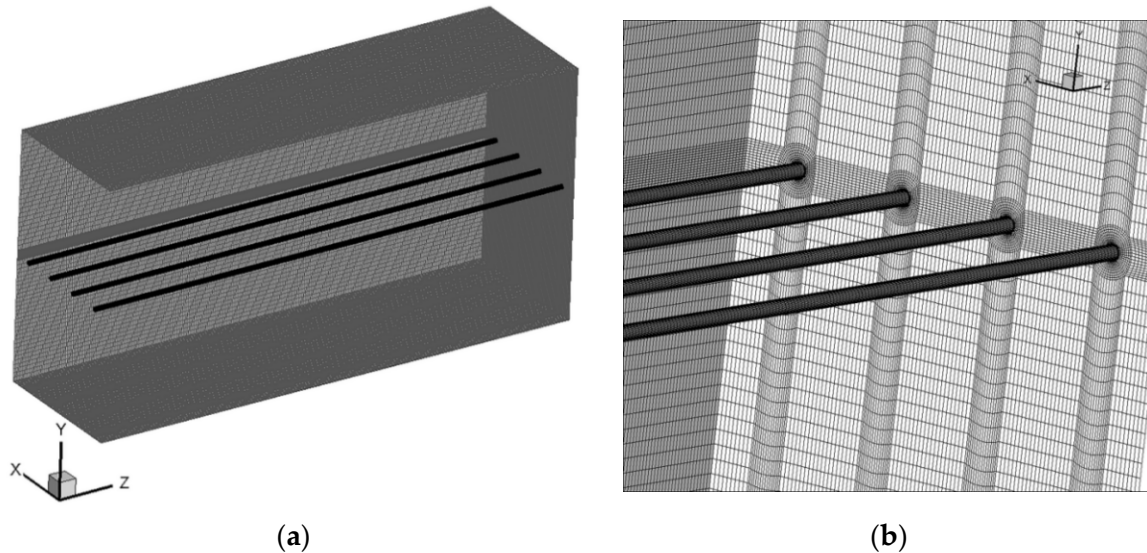


Figure 12. Schematic diagram of meshing. (a) Overall grid layout and (b) Local grid layout.

Four different grid schemes were selected for simulation, corresponding to 3,480,001, 4,216,800, 5,608,400, and 6,048,400 grid cells, respectively. To analyze grid independence [22,23], as shown in Figure 13, the corresponding temperatures of the same monitoring points after simulation for 6 h, under different numbers of grid cells, were verified. The temperatures of the monitoring points corresponding to 5,608,400 and 6,048,400 grid cells were both 25.67 °C. The error between these two simulated grid schemes was small and the simulations were stable. Therefore, the grid division scheme with 5,608,400 grid cells was selected.

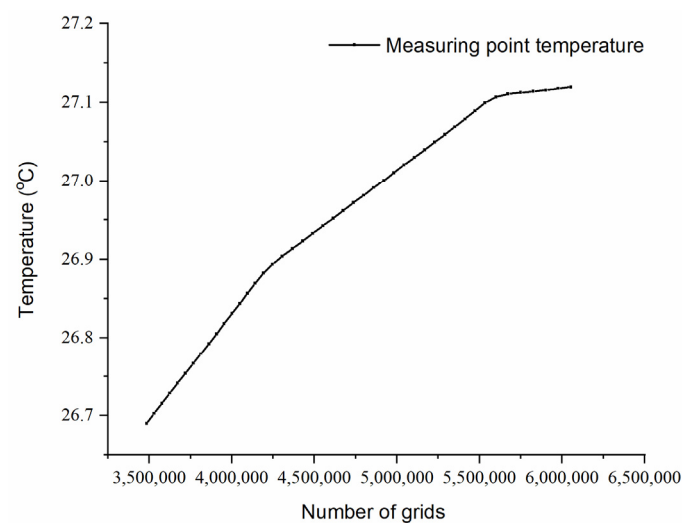


Figure 13. Grid independence analysis assessment.

2.4.4. Boundary Condition

The heat transfer at the soil surface should take into account both the convective heat transfer between the surface and the air and solar radiation received by the surface.

Therefore, it was assumed that the sensible heat source on the surface is a certain percent of the solar radiation incident on the soil surface, so the solar radiation was simplified as an internal heat source on the soil surface with a thickness of 0.005 m that changes over time [12,16]. That is to say, the soil surface was set as the third type boundary condition with an internal heat source; α_s in Equation (10) is set as 0.33 and the convective heat transfer coefficient is 4.0 W/(m²·K) during the day and 7.0 W/(m²·K) at night [12,16].

As shown in Figure 11, the boundary of the heating pipe acts as the heat transfer interface between the fluid and soil computational domains, and its heat transfer is affected by two computational domains. Therefore, this wall surface was set to a coupled wall boundary condition. The inlet of the heating pipe is the velocity inlet, and the velocity and temperature at the inlet boundary are given. When the system is in operation, the inlet flow rate is 0.051 m/s. When the system is shut down, the inlet speed of the heating pipe is zero. The inlet temperature of the heating pipe is the outlet water temperature of the heat storage tank. The outlet boundary of the heating pipe was set to a free outflow boundary condition. The bottom soil of the model was set to the first type of boundary condition, i.e., it is assumed that the soil layer at a depth of 1400 mm has a constant temperature of 12 °C. The surrounding soil surface boundaries were set as adiabatic boundaries.

The shallow soil temperature changes according to various parameters, and the initial soil temperature can be calculated according to Equation (14) [24].

$$T(\tau, Z) = T_m + A_w e^{-Z\sqrt{\frac{\pi}{aP}}} \cos\left(\frac{2\pi}{P}(\tau - \tau_0) - Z\sqrt{\frac{\pi}{aP}}\right) + T_{ad} \quad (14)$$

where $T(\tau, Z)$ is the soil temperature at different times and depths, °C; τ is the time, h; Z is the soil depth, m; T_m is the annual average soil surface temperature, °C; A_w is the periodic fluctuation amplitude of soil surface temperature, °C; P is the annual fluctuation period of soil temperature, h, at $P = 365 \times 24 = 8760$ h; τ_0 is the time when the soil temperature reaches its maximum, h; a is the thermal diffusivity of soil, m²/h; T_{ad} is additional temperature depending on surface conditions, °C and 0 °C for bare ground and 1 °C for gassy ground.

For the case in Jinan, $T_m = 15.7$ °C, $A_w = 17$ °C, $a = 0.00318$ m²/h, and $T_{ad} = 1$ °C, when tomatoes were grown in a greenhouse. These values were substituted into Equation (14) to calculate the soil temperature at different depths corresponding to the initial time of simulation (0:00 on 25 September 2019). The initial soil temperature is fitted into a function related to depth Z , as shown in Figure 14, and the fitting formula is as follows.

$$T_Z = -1.053Z^2 - 1.593Z + 298.523 \quad (15)$$

where T_Z is soil temperature at a specific depth, K.

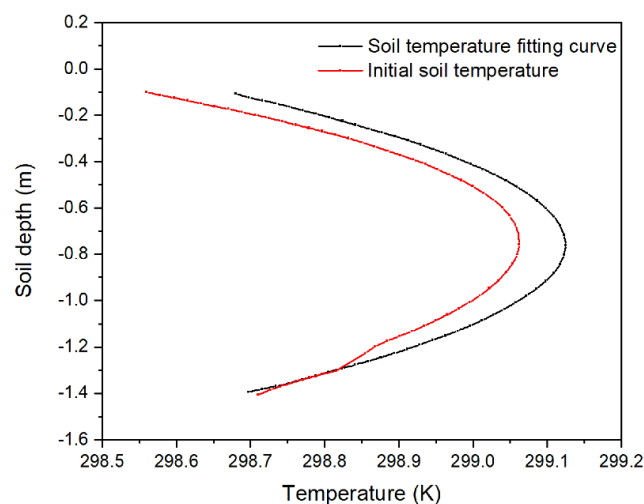


Figure 14. Fitting curve of initial soil temperature.

2.4.5. Parameter Set Up and Numerical Scheme

In Jinan, the soil density is 1925 kg/m^3 , the specific heat capacity is $920 \text{ J/(kg}\cdot\text{K)}$, and the thermal conductivity is $1.6 \text{ W/(m}\cdot\text{K)}$. The density of the PE-RT horizontal heating pipe is 1200 kg/m^3 , its specific heat capacity is $1380 \text{ J/(kg}\cdot\text{K)}$, and its thermal conductivity is $0.31 \text{ W/(m}\cdot\text{K)}$. Other transient parameters, such as air temperature, internal heat source intensity, fluid temperature, fluid velocity, and heat transfer coefficient of soil surface, are compiled into time-related profile files, which are read and loaded into each boundary condition by the ANSYS Fluent software.

To ensure convergence of the numerical simulation, the SIMPLEC (Simple Consistent) algorithm in the separated solver was selected for calculation. This algorithm is an improvement on the Semi-Implicit Method for Pressure-Linked Equations. The diffusion term in the governing equation is discretized by a central difference scheme, and the convection term is discretized by a second-order upwind scheme. The variation in the residuals is checked, and the most reasonable under-relaxation factor is selected. The User-Defined Function is adopted to initialize the soil temperature field according to Equation (14). The time step was set to 200 s.

2.4.6. Model Validation

The measured and simulated soil temperature curves at depths of 15 cm and 30 cm at 0:00 during the transition season, September 25 to November 14, are compared in Figure 15. The figure shows that most of the simulated soil temperature values were higher than the measured values. This may have been because there were errors in the assumptions regarding solar radiation as a heat source on the soil surface; or because there were errors in the values assigned to the convective heat transfer coefficient between the soil surface and air inside the greenhouse. In summary, the relative errors [25] between the simulated and measured soil temperature at 15 cm and 30 cm depths were within 10%, which indicated that the established model of the horizontal heating pipe and surrounding soil temperature field is reliable and can be used to simulate underground soil temperature fields.

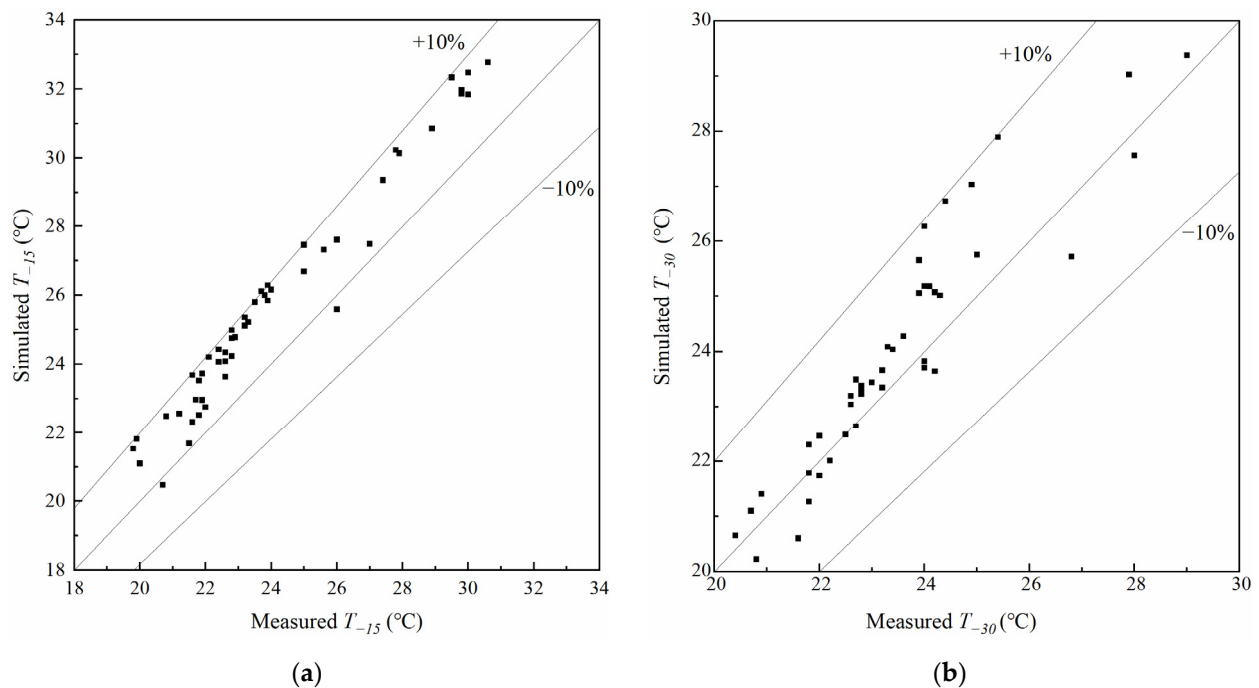


Figure 15. Measured and simulated soil temperatures during the transition season. (a) T_{-15} and (b) T_{-30} .

2.5. Typical Operating Conditions

Combined with the measured data, the continuous change in the soil temperature field during the experimental period was simulated. Operating conditions for typical weeks, typical sunny days, and cloudy days were extracted and analyzed. The meteorological parameters of each typical time period are shown in Table 3. Among them, the typical week, i.e., 11–16 December 2019, included both sunny days and rainy days, making it representative.

Table 3. Typical daily meteorological parameters.

Case	Date	Weather	Lowest Outdoor Temperature (°C)	Highest Outdoor Temperature (°C)
Typical week	11 December 2019	Sunny	−3	9
	12 December 2019	Sunny	0	10
	13 December 2019	Cloudy	0	12
	14 December 2019	Cloudy	0	8
	15 December 2019	Light rain	4	6
	16 December 2019	Light rain	1	6
	17 December 2019	Cloudy	0	6
Typical cloudy day in transition season	24 October 2019	Cloudy	7	17
Typical sunny day in transition season	8 November 2019	Sunny	7	23
Typical sunny winter days	27 December 2019	Sunny	−3	9
	28 December 2019	Sunny	2	13
Typical cloudy winter days	5 January 2020	Snow and Rain	1	3
	6 January 2020	Fog and Snow	−1	2

3. Results

3.1. Experimental Results

3.1.1. Soil Temperature

The soil temperatures at depths of 15 cm and 30 cm at 00:00 from 23 September 2019, to 8 March 2020, are plotted in Figure 16. As can be seen, the soil temperature increased in the early stages of heat storage, but after October, the soil temperature gradually decreased with the decreasing air temperature. The soil temperature at depths of 15 cm and 30 cm were mostly higher than 20 °C before 23 November 2019. T_{-15} dropped to its lowest point, i.e., 14 °C, during the week from 7 January to 14 January 2020, while T_{-30} dropped to its lowest point, i.e., 14 °C, on 17 January 2020. Beginning 9 February 2020, the soil temperature gradually increased. When the air temperature was high and the sunshine was sufficient, because the soil at a 15 cm depth absorbs more solar radiation, its temperature was higher than that at a 30 cm depth. Conversely, when the air temperature was low or the sunshine insufficient, the soil temperature at a 30 cm depth was higher than that at a 15 cm depth, and the thermal hysteresis of solar radiation and air temperature became more obvious.

3.1.2. Water Temperature

In order to clearly present the relationship between water temperature and the activation/inactivation of the pump, that data from typical weeks were selected for analysis, as shown in Figure 17. The figure shows that on sunny days, e.g., December 11 and December 12, once the temperature difference between the water temperature in the collector and the soil at 15 cm depth exceeded 7 °C, the circulating water pump was activated and ran continuously for about 6.5 h, from 9:20 to 15:50. On typical cloudy days, the circulating pump operated for less time, e.g., for 1 h on December 14, and briefly on December 15 and

16. The fluctuations in soil temperature at depths of 15 cm and 30 cm were small, ranging from 16 °C to 18 °C. Due to the low outside temperatures, the soil temperature at a 15 cm depth was lower than that at a 30 cm depth.

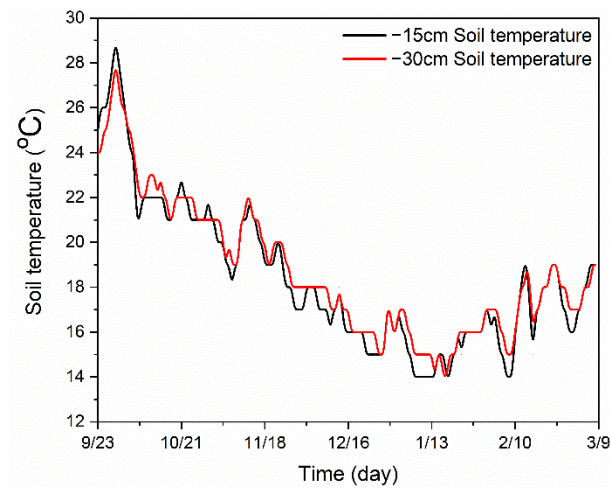


Figure 16. Soil temperature at 15 cm and 30 cm depths at 0:00 during the experimental period.

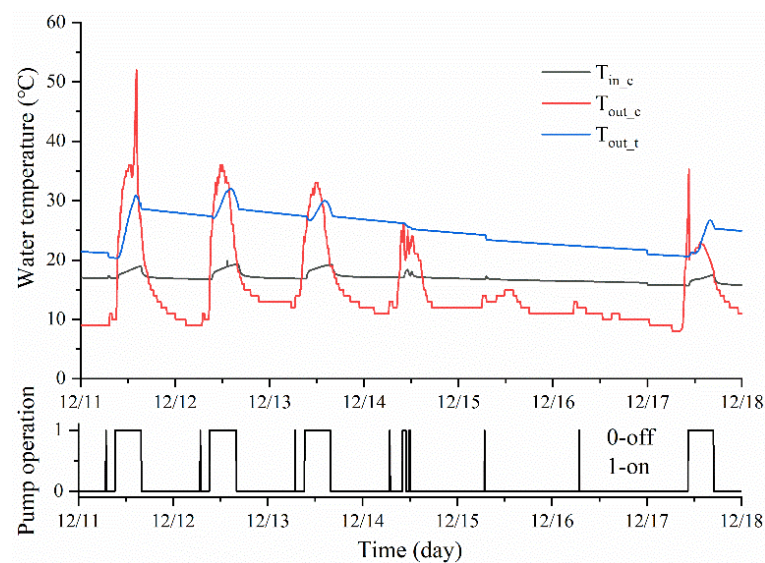


Figure 17. Experimental data of water temperature and pump operation time from 11 December to 17 December 2019.

3.1.3. Solar Collector Efficiency and COP

System performance parameters during typical days and the whole experimental period are shown in Table 4. The table shows that, due to the large temperature difference between the heating pipes and soil caused by sufficient sunshine and low soil temperatures, the max heat collection efficiency and COP occurred on sunny winter days (December 27–28). However, on cloudy winter days (January 5–6), the water temperature in the heating pipe was too low to release heat to the soil, so the heat dissipation to the soil was less than zero, and COP was taken as zero.

Table 4. Performance indexes on typical days.

Date	Solar Radiation (kWh)	Solar Energy Collected (kWh)	Heat Released to Soil (kWh)	Pump Energy Consumption (kWh)	Solar Collector Efficiency (%)	COP
11–17 December	882.26	299.97	276.29	5.65	34	48.90
24 October	118.89	60.53	24.17	0.90	51	26.86
8 November	315.64	207.31	117.67	2.03	66	58.11
27–28 December	413.07	318.00	281.70	3.63	77	77.60
5–6 January	57.87	10.80	0	0.02	19	0
23 September–8 March	32,594.87	15,277.13	15,107.55	223.15	47	67.70

Moreover, from 23 September 2019 to 8 March 2020, the average COP of the active solar heating system was about 67.70, much higher than that of the traditional energy system, indicating that this system is a feasible soil heating method for cold regions.

3.2. Simulation Results in the Transition Season

Figure 18 shows the simulated soil temperature distribution at sections $z = -15$ m, $z = -50$ m, and $x = 0.3$ m at 0:00 on 24 October 2019, a typical cloudy day in the transition season. It can be seen that heat accumulates in the soil along the positive Y-axis directions. Figure 18a shows that soil temperature becomes significantly stratified in the positive Y-axis direction, and that soil temperature decreased with increasing depth. Due to the interaction of heat transfer from multiple heating pipes, the isotherms near the heating pipes appear wavy.

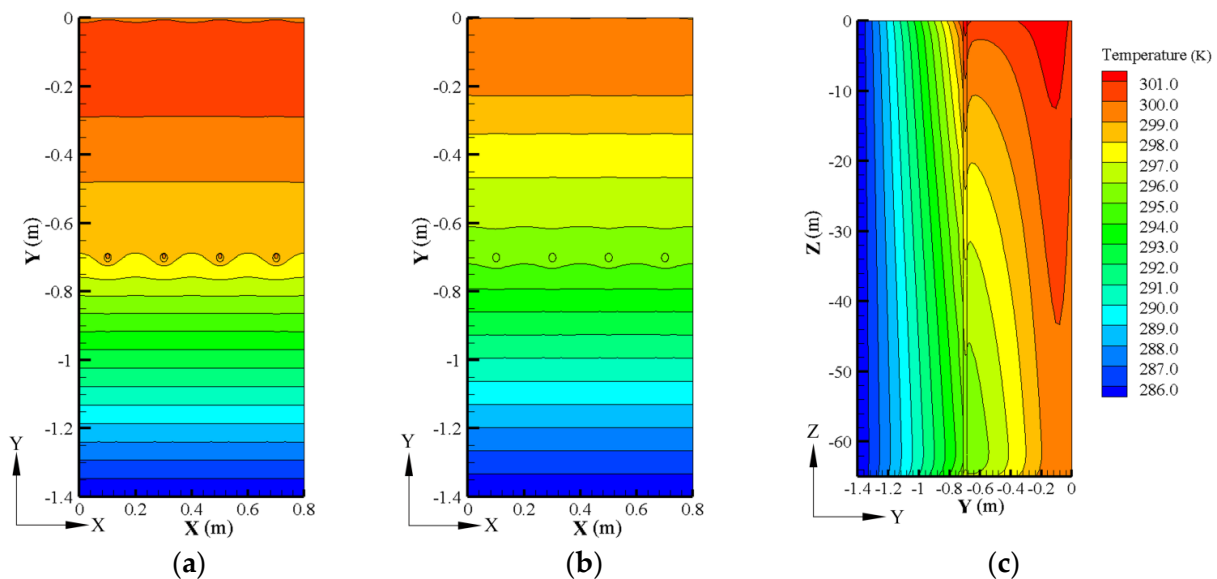


Figure 18. Simulated soil temperature distribution at 0:00 on 24 October 2019. (a) $Z = -15$ m, (b) $Z = -50$ m, and (c) $X = 0.3$ m (the X-to-Y ratio is set as 20).

By comparing Figure 18a,b, it can be seen that, under the combined action of solar radiation and upward heat flow from the fluid in the heating pipe, the soil temperature gradient above the heating pipe increases along positive X-axis. The variation in soil temperature gradient below the heating pipes is small and the isotherms are denser, revealing that heating pipes have a limited influence on the soil below them.

As Figure 18c shows, the fluid in the pipe dissipates heat to the soil along the direction of flow, and the fluid temperature and soil temperature gradually decrease along the positive X-axis as the heat exchange decreases. The highest soil temperature was 27.85 °C and the lowest was 23.85 °C at the plough layer 60 cm below the surface.

Figure 19 shows the simulated soil temperature distribution at sections $Z = -15$ m, $Z = -50$ m, and $X = 0.3$ m at 0:00 on 8 November 2019, a typical sunny day in the transition season. Compared with Figure 18, the soil temperature is lower, but as heat

storage progressed, the action area of the heating pipe on the upper soil field expands, the soil temperature gradient decreases, and the soil isotherm becomes sparse. The thermal coupling between heating pipes is enhanced, and the wavy isotherms also appear near the heating pipes at the $Z = -50$ m section. The highest soil temperature was 24.85 °C and the lowest was 21.85 °C at the depth of 60 cm.

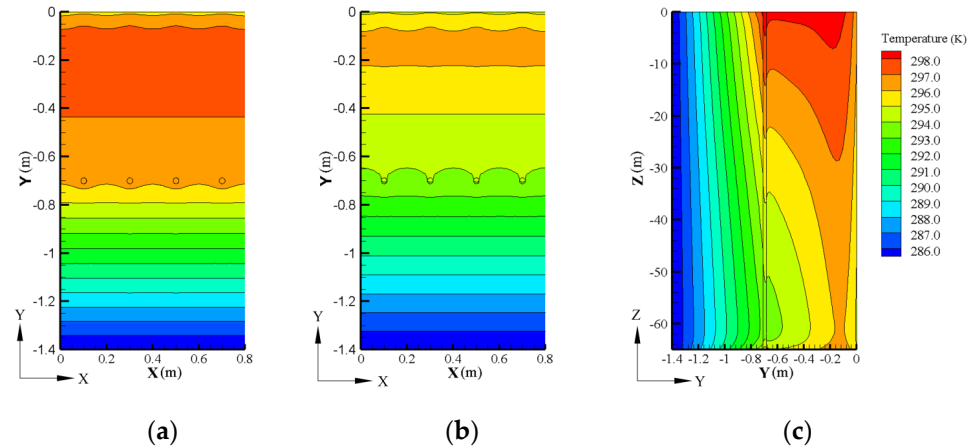


Figure 19. Soil temperature distribution at 0:00 on 8 November 2019. (a) $Z = -15$ m, (b) $Z = -50$ m, and (c) $X = 0.3$ m (the X-to-Y ratio is set as 20).

3.3. Simulation Results in Typical Sunny Winter Days

Figure 20 shows the simulated soil temperature distribution at sections $z = -15$ m, $z = -50$ m, and $x = 0.3$ m at 4:00 on December 27, a typical sunny day in winter. By comparing Figure 20a,b, it can be seen that the soil temperature is higher and the soil temperature gradient is larger at the $z = -15$ m section than that at the $z = -50$ m section. Compared with the performance during night in the transition season in Figure 18, the surface soil is cooled more during night in winter due to the release of heat to the low-temperature air, and the lowest temperature of the surface soil reached about 15.56 °C. Figure 20c shows that, after the shutdown of the circulating pump, the heating pipe gradually approaches thermal equilibrium with the surrounding soil, and the water temperature still decreases along positive X-axis and decreases rapidly. The maximum soil temperature at the $z = -50$ m section is 1.9 °C lower than at the $z = -15$ m section. At night in winter, after the pump turned off, the soil temperature at a 60 cm depth becomes relatively uniform at around 16.85 °C for the length of the greenhouse, with the lowest temperature being 16.20 °C.

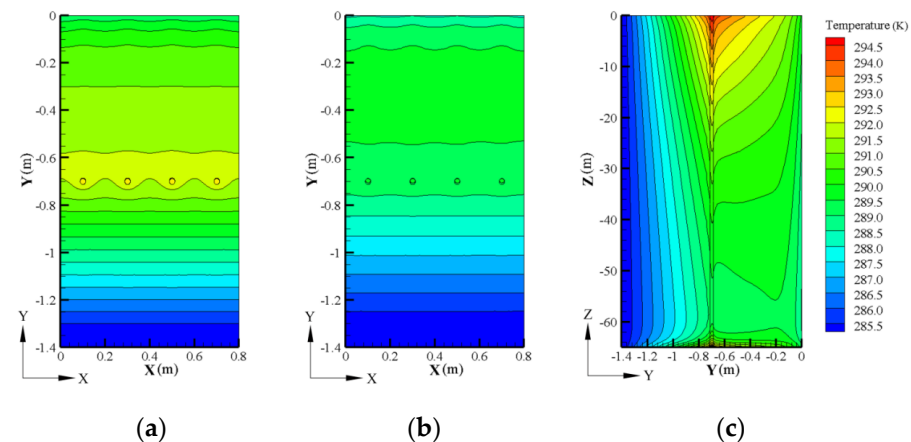


Figure 20. Soil temperature distribution at 4:00 on 27 December 2019. (a) $Z = -15$ m, (b) $Z = -50$ m, and (c) $X = 0.3$ m (the X-to-Y ratio is set as 20).

Figure 21 shows simulated soil temperature distributions at the $Z = -15$ m, $Z = -50$ m, and $X = 0.3$ m sections at 16:00 on December 27, in the afternoon on a sunny day in winter. It can be seen that, due to the increased solar radiation and indoor temperature during the day, the soil temperature 10 cm below the surface increases significantly compared to night, with the highest temperature reaching 19°C . Strong sunshine in the daytime increases the water temperature in the heating pipe, and the thermal action range along the positive Y -axis is greater than at night. The soil temperature under the heating pipes rises slightly compared with the temperatures at night. The highest soil temperature was 19.42°C and the lowest was 16.21°C at the depth of 60 cm.

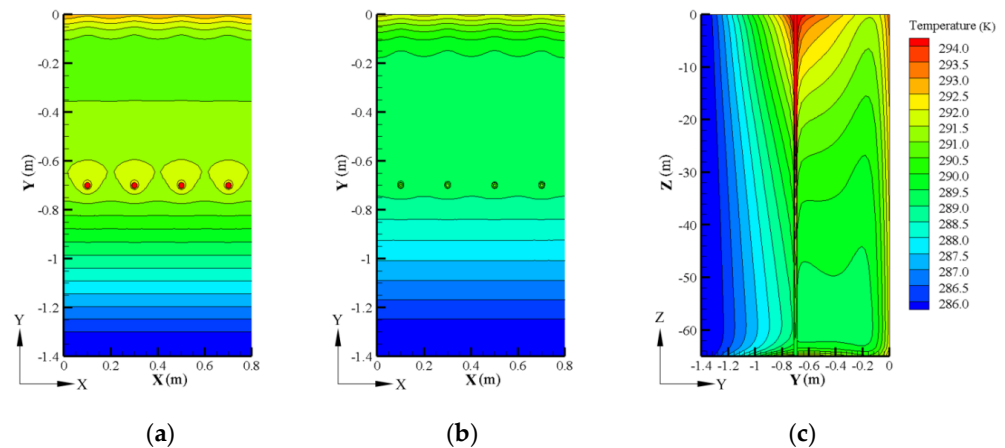


Figure 21. Soil temperature distribution at 16:00 on 27 December 2019. (a) $Z = -15$ m, (b) $Z = -50$ m, and (c) $X = 0.3$ m (the X-to-Y ratio is set as 20).

The simulated soil temperatures at different depths on typical sunny winter days are shown in Figure 22. The hysteresis and attenuation of soil temperature fluctuation increases with depth. Solar radiation and air temperature have great impacts on shallow soil at depths of 10 cm and 15 cm, but little impact on the soil at 30 cm and almost no impact on the soil at depths from 40 to 60 cm. Since no auxiliary heat sources are set up in the greenhouse, the shallow soil on the surface releases heat to the air in the greenhouse at night. Therefore, the soil temperatures at depths of 10 cm are lower than those at 15 cm, and the temperature difference decreases when the air temperature increases.

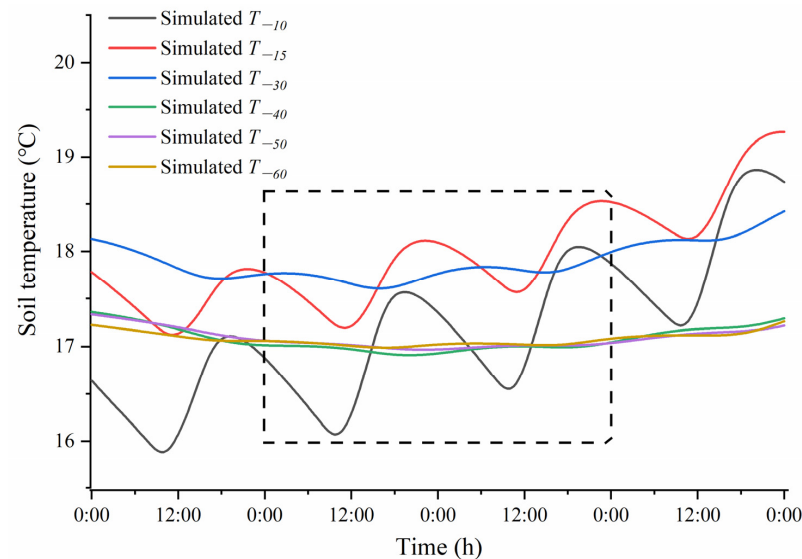


Figure 22. Soil temperature at different depths on sunny winter days (dashed box represents the soil temperatures on cloudy days, $Z = -30$ m).

3.4. Simulation Results in Typical Cloudy Winter Days

Figure 23 shows the simulated soil temperature distributions at the $Z = -15$ m, $Z = -50$ m, and $X = 0.3$ m sections at 4:00 on 6 January 2020, a typical rainy and snowy day in winter. As can be seen from the figure, a low temperature at night has the most pronounced influence on the surface soil temperature. The overall trend of soil temperature gradually decreases along the axis of the heating pipe center, but the heating pipe near the water inlet still has a thermal effect on the 40 cm of soil above it. The isotherms above and below the heating pipes smoothly transition into each other.

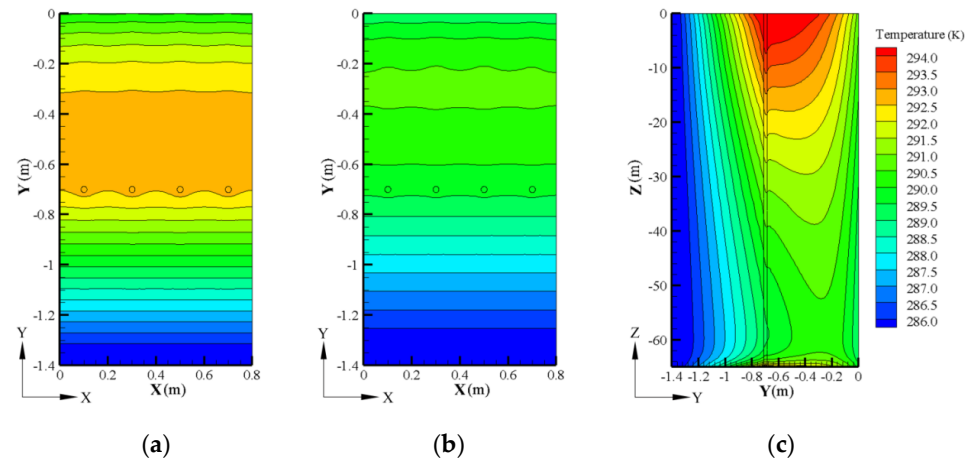


Figure 23. Soil temperature at 4:00 on 6 January 2020. (a) $Z = -15$ m, (b) $Z = -50$ m, and (c) $X = 0.3$ m (the X-to-Y ratio is set as 20).

Figure 24 shows the soil temperature fields at the $Z = -15$ m, $Z = -50$ m, and $X = 0.3$ m sections at 16:00 on 6 January 2020. Compared with Figure 23, the thermal effect of the heating pipe on the soil above it tends to decrease, the water temperature and soil temperature at the inlet of the heating pipe decrease, and the soil surface temperature decreases.

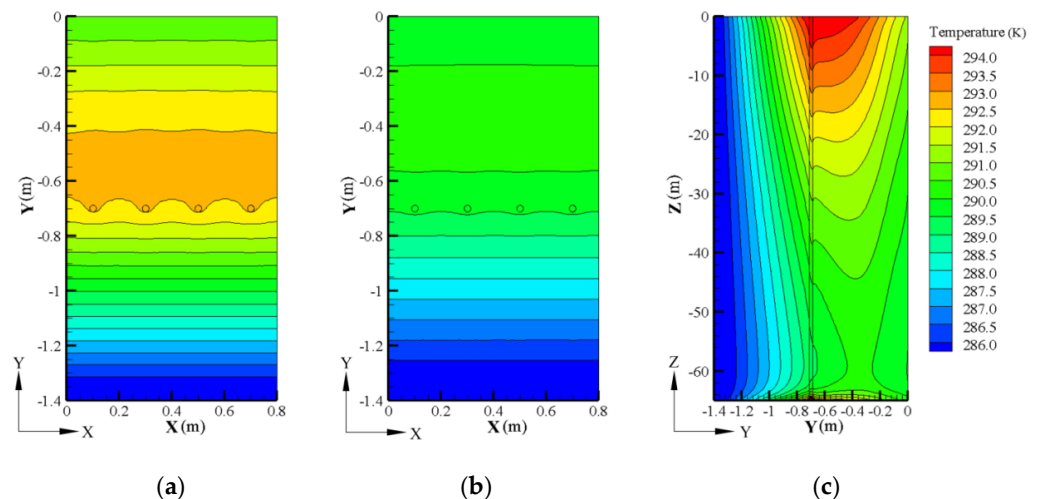


Figure 24. Simulated soil temperature distribution at 16:00 on 6 January 2020. (a) $Z = -15$ m, (b) $Z = -50$ m, (c) $X = 0.3$ m (the X-to-Y ratio is set as 20).

Note that Figures 22a and 24a presented the temperature contour at the section of $Z = -15$ m, which is close to the inlet of the heating pipe. Moreover, the heating pipe located at the depth of 70 cm inside the soil, correspondingly, and the location of T_{-60} at the depth of 60 cm in the soil, are closer to the heating pipe than the location of T_{-30} at

the depth of 30 cm. Therefore, due to the different section locations for the temperature contour, the soil temperature between Figure 22a, Figure 24a, and Figure 25 may have a slight temperature difference compared to the T_{-60} and T_{-30} . When hot water flows into the heating pipe, the soil close to the water inlet and the heating pipe will preferentially absorb heat, resulting in that T_{-60} is a little higher than T_{-30} at $Z = 15$ m. With the fluid flow and heat loss in the heating pipe, this situation will be changed.

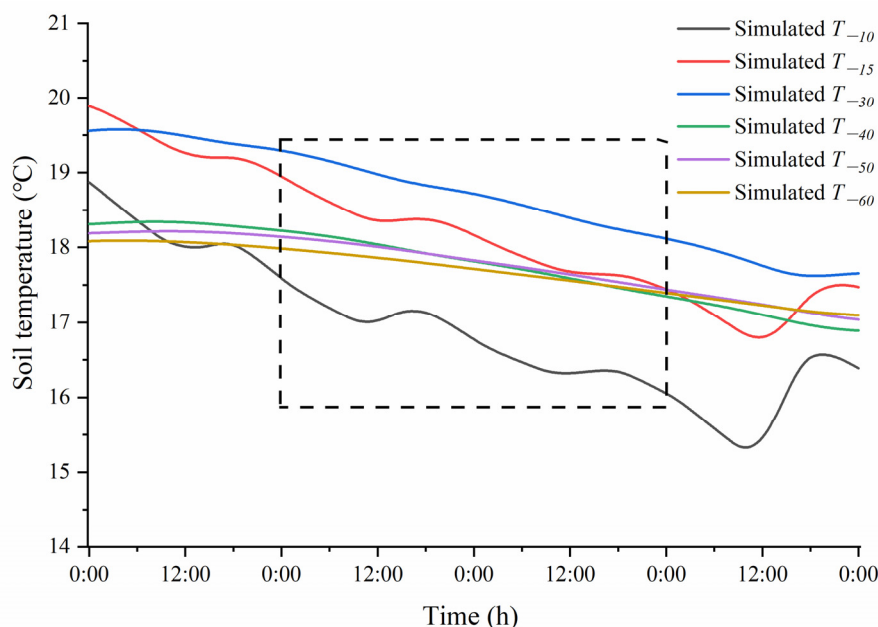


Figure 25. Soil temperature at different depths on snowy winter days (dashed box represents the soil temperature on cloudy days, $Z = -30$ m).

Figure 25 shows the changes in soil temperature at different depths from 5–6 January 2020. Clearly, the soil temperatures at all depths show downward trends. The soil temperature at the 10 cm and 15 cm depths are significantly correlated with the air temperature in the greenhouse, and exhibit the largest temperature drop about 1.5 °C. The soil temperature at a 30 cm depth is the highest, and the soil temperature between a 40–60 cm depth decreases slowly.

4. Discussion

In the Jinan City, located in the cold climate zone, an active solar heating system was proposed, and an experimental system was established. The experiment lasted for nearly six months. At first, the complete experiment, including heat collection, heat storage, and heat release, were carried out, and the performance of the system was effectively analyzed. Then, the operation strategy of the system was obtained, which will help to improve the applicability of this system in cold climate zones, and it indicated the important practical significance.

During the installation of the solar collector in this project, in order not to block sunlight from reaching the rear of the greenhouse, the collector was affixed to the back wall of the greenhouse. The attenuation of solar irradiance caused by the EVA film of the greenhouse is about 34.2%, which results in a reduction in the effective heat collected and effective heat stored in the soil. In follow-up research and applications, the installation of the collector should be taken into account in the greenhouse construction stage, so that the collector can be integrated into the greenhouse design and solar radiation per unit area can be maximized. In addition, the heat load of the experimental solar greenhouse was 595,96.2 W, equivalent to a heat index per unit area of 77.4 W/m². To improve the thermal insulation of the greenhouse and reduce its heat loss in winter, a semi-underground type of envelope with thicker walls and thicker insulation layers throughout is recommended.

This experiment only placed temperature sensors at 15 cm and 30 cm depths, which meant that the deeper soil was not monitored. In order to explore the soil temperatures at various depths around the plant roots, a simulation was carried out, and the experimental data were input into the simulation model. By comparing the measured and simulated values of soil temperatures at 15 cm and 30 cm depths, the simulation model was verified. This meant that the simulated soil temperatures at 40 cm, 50 cm, and 60 cm depths were reasonably accurate.

When establishing the simulation mathematical model, the boundary conditions were simplified. Solar radiation was assumed to be the heat source to the soil surface, and the convective heat transfer coefficient between the soil surface and air was taken as a fixed value that changed only between day and night. The effects of plant transpiration, soil heat, and moisture transfer were not taken into account. For a more accurate mathematical model, the above factors need to be comprehensively considered.

Moreover, the solar greenhouse with the same structure and without any auxiliary heating source should be used for the benchmark comparison in the future, in order to illustrate the benefits of this active heating system. The soil temperature at the different depths should be tested in details, and the plant growing status should be paid close attention to. For the greenhouse without an active heating system, a mathematical model considering both of the heat transfer inside the greenhouse and soil may also be established for benchmark comparison analysis.

In addition, in order to retain heat during the experiment, a thermal insulating cotton blanket was extended to cover the EVA film at night and retracted after the sun rose the next day. One hour after the blanket was extended each night, a limited ventilation was conducted for 7–8 min. All these operations affected the indoor temperature and humidity, and subsequently affected the heat transfer process between the soil surface and indoor air. However, since soil temperatures around plant roots were the focus of this paper, the influences of the thermal insulation blanket and ventilation were ignored. Therefore, further studies will take into account those factors.

For the experimental solar greenhouse described in this paper, the existing active solar heating system was able to maintain a reasonable soil temperature on rainy and snowy days in winter to prevent crop growth from being inhibited. However, for thermophilic crops such as tomatoes, it may still be necessary to increase the air temperature in the greenhouse on cold nights using auxiliary heat sources such as biomass energy, to sustain root temperatures in the more suitable growth range of 20–22 °C. To minimize dependence on fuel consuming systems, the operation of auxiliary heat sources based on active solar heating systems needs to be further studied.

5. Conclusions

Using experiments and three-dimensional numerical simulations on an active solar heating system integrated into a greenhouse, the following conclusions could be made.

During the experimental period from 23 September 2019, to 8 March 2020, the effective heat collection of the solar collector was 15,268.49 kWh, the heat storage of the soil was 15,107.55 kWh, and the power consumption of the pump was 223.15 kWh. The efficiency of the solar collector efficiency came to 47% and the COP was 67.70. Compared with traditional energy systems, this active solar heating system had outstanding advantages in thermal economy.

The soil temperatures at depths of 15 cm and 30 cm were significantly correlated with the air temperature in the greenhouse. Soil temperatures gradually decreased with decreasing air temperatures from October 2019 to January 2020, until February 2020, when the temperatures started to rise again. In order to alleviate the temperature drop in the cold winter more effectively, the heat storage time can be shifted to an early date and a longer period.

Strong sunshine increases the water temperature in the heating pipes. As the heat is transferred to the soil, the actively increasing temperature field in the soil above the heating

pipe expands, and the thermal coupling between heating pipes is strengthened. On cloudy winter nights, the shallow soil cooled down due to heat dissipating into the air, but the magnitude of the reduction in soil temperature decreased with depth. The heating pipe had a limited influence on the underlying soil, so heating pipes should be positioned below the main root system of the crop.

The simulated root zone temperature in winter ranged from 16.06 °C to 18.95 °C. The active solar heating system had a clear warming effect on soil temperature in the cold winter, and it would be able to maintain soil temperature and prevent the inhibition of plant growth caused by low soil temperatures. This system has great potential in soil heating applications in cold regions.

Author Contributions: Conceptualization, T.Y.; methodology, T.Y., J.L. and M.K.K.; software, T.Y. and D.W.; validation, T.Y. and J.L.; formal analysis, T.Y.; investigation, T.Y. and J.L.; resources, T.Y. and J.L.; data curation, T.Y. and D.W.; writing—original draft preparation, T.Y. and D.W.; writing—review and editing, X.Z., J.L. and M.K.K.; visualization, T.Y., D.W. and X.Z.; supervision, J.L.; project administration, J.L.; funding acquisition, T.Y. and J.L. All authors have read and agreed to the published version of the manuscript.

Funding: The paper is supported by Natural Science Foundation of Shandong Province (ZR2019MEE083).

Acknowledgments: The paper is supported by Natural Science Foundation of Shandong Province (ZR2019MEE083). This work was also supported by the Plan of Introduction and Cultivation for Young Innovative Talents in Colleges and Universities of Shandong Province.

Conflicts of Interest: The authors declare no conflict of interest.

Nomenclature

A	solar collector area (m ²)
A_w	periodic fluctuation amplitude of soil surface temperature (°C)
a	thermal diffusivity of soil (m ² /h)
c	specific heat capacity (J/(kg·°C))
h_c	convective heat transfer coefficient between soil surface and air (W/(m ² ·°C))
I	solar radiation intensity (W/m ²)
i	incident angle
k	thermal conductivity (W/(m·K))
m_c	mass flow (kg/s)
N	pump power (W)
P	annual fluctuation of soil temperature (h)
p	pressure (Pa)
Q_A	total solar radiant energy received by the collector (W)
Q_U	effective heat collection of collector (W)
q	heat flux (J/(m ² ·s))
R	ratio of the reflected radiation to the incident radiation
T	temperature (°C)
T_m	annual average soil surface temperature (°C)
t	time (s)
Z	soil depth (m)

Abbreviation

CFD	computational fluid dynamics
COP	coefficient of performance
EVA	ethylene vinyl acetate copolymer

Greek symbols

α_s	absorptivity of the ground toward solar radiation
β	collector installation inclination
θ	total solar radiation
λ	thermal conductivity of soil (W/(m·K))
μ	dynamic viscosity (Pa·s)
ρ	density (kg/m ³)
τ	time since start time of work (s)

Subscripts

a	air
ad	additional
av	average
b	direct solar radiation
c	constant
d	scattered solar radiation
f	fluid
g	ground
out_c	outlet of solar collector
out_t	outlet of water storage tank
r	reflected solar radiation
s	soil
–15	soil at 15 cm depth
–30	soil at 30 cm depth

References

- Liu, H.; Yin, C.; Hu, X.; Tanny, J.; Tang, X. Microclimate Characteristics and Evapotranspiration Estimates of Cucumber Plants in a Newly Developed Sunken Solar Greenhouse. *Water* **2020**, *12*, 2275. [[CrossRef](#)]
- Dong, S.; Ahamed, S.; Ma, C.; Guo, H. A Time-Dependent Model for Predicting Thermal Environment of Mono-Slope Solar Greenhouses in Cold Regions. *Energies* **2021**, *14*, 5956. [[CrossRef](#)]
- Wei, X.; Li, Y.; Fan, X.; He, C.; Yan, Y.; Sun, M.; Ding, C.; Wang, J.; Yu, X. Techno-Economic Feasibility of In Situ Vegetable Residue Return in the Chinese Solar Greenhouse. *Agronomy* **2021**, *11*, 1828. [[CrossRef](#)]
- Cai, B.; Ning, Y.; Li, Q.; Li, Q.; Ai, X. Effects of the Chloroplast Fructose-1,6-Bisphosphate Aldolase Gene on Growth and Low-Temperature Tolerance of Tomato. *Int. J. Mol. Sci.* **2022**, *23*, 728. [[CrossRef](#)] [[PubMed](#)]
- Wang, Y.; Lu, Y.; Xiao, R. Application of Nonlinear Adaptive Control in Temperature of Chinese Solar Greenhouses. *Electronics* **2021**, *10*, 1582. [[CrossRef](#)]
- Gorjian, S.; Calise, F.; Kant, K.; Ahamed, S.; Copertaro, B.; Najafi, G.; Zhang, X.; Aghaei, M.; Shamshiri, R.R. A review on opportunities for implementation of solar energy technologies in agricultural greenhouses. *J. Clean. Prod.* **2021**, *285*, 124807. [[CrossRef](#)]
- Lazaar, M.; Bouadila, S.; Kooli, S.; Farhat, A. Comparative study of conventional and solar heating systems under tunnel Tunisian greenhouses: Thermal performance and economic analysis. *Sol. Energy* **2015**, *120*, 620–635. [[CrossRef](#)]
- Kurpaska, S.; Slipek, Z. Optimization of Greenhouse Substrate Heating. *J. Agric. Eng. Res.* **2000**, *76*, 129–139. [[CrossRef](#)]
- Bernier, H.; Raghavan, V.; Paris, J. Evaluation of a soil heat exchanger-storage system for a greenhouse. Part I: System performance. *Can. Agr. Eng.* **1991**, *33*, 93–98.
- Attar, I.; Farhat, A. Efficiency evaluation of a solar water heating system applied to the greenhouse climate. *Sol. Energy* **2015**, *119*, 212–224. [[CrossRef](#)]
- Zhang, L.; Xu, P.; Mao, J.; Tang, X.; Li, Z.; Shi, J. A low cost seasonal solar soil heat storage system for greenhouse heating: Design and pilot study. *Appl. Energy* **2015**, *156*, 213–222. [[CrossRef](#)]
- Joudi, K.A.; Farhan, A. A dynamic model and an experimental study for the internal air and soil temperatures in an innovative greenhouse. *Energy Convers. Manag.* **2015**, *91*, 76–82. [[CrossRef](#)]
- Awani, S.; Kooli, S.; Chargui, R.; Guizani, A. Numerical and experimental study of a closed loop for ground heat exchanger coupled with heat pump system and a solar collector for heating a glass greenhouse in north of Tunisia. *Int. J. Refrig.* **2017**, *76*, 328–341. [[CrossRef](#)]
- Attar, I.; Naili, N.; Khalifa, N.; Hazami, M.; Farhat, A. Parametric and numerical study of a solar system for heating a greenhouse equipped with a buried exchanger. *Energy Convers. Manag.* **2013**, *70*, 163–173. [[CrossRef](#)]
- Gauthier, C.; Lacroix, M.; Bernier, H. Numerical simulation of soil heat exchanger-storage systems for greenhouses. *Sol. Energy* **1997**, *60*, 333–346. [[CrossRef](#)]
- Tong, G.; Li, B.; Christopher, D.; Yamaguchi, T. Preliminary study on temperature pattern in China solar greenhouse using computational fluid dynamics. *Trans. Chin. Soc. Agric. Eng.* **2007**, *23*, 178–185.

17. Dong, X. Evaluation of Solar Energy Resources in Shandong Province. Master's Thesis, Lanzhou University, Lanzhou, China, May 2009.
18. He, Z. *Solar Thermal Utilization*; China University of science and Technology Press: Hefei, China, 2009.
19. Zang, Y. Application of Solar Assisted Heating Technology in Heating System. Master's Thesis, North China Electric Power University, Beijing, China, December 2011.
20. Zhang, H.F. *Principle of Solar Thermal Utilization and Computer Simulation*; Northwestern Polytechnical University Press: Xi'an, China, 2012.
21. Duffie, J.A.; Beckman, W.A.; Worek, W.M. *Solar Engineering of Thermal Processes*, 4th ed.; John Wiley & Sons, Inc.: Hoboken, NJ, USA, 2013; p. 928.
22. Liu, J.; Li, Z.; Kim, M.K.; Zhu, S.; Zhang, L.; Srebric, J. A comparison of the thermal comfort performances of a radiation floor cooling system when combined with a range of ventilation systems. *Indoor Built Environ.* **2020**, *29*, 527–542. [[CrossRef](#)]
23. Liu, J.; Zhu, S.; Kim, M.K.; Srebric, J. A Review of CFD Analysis Methods for Personalized Ventilation (PV) in Indoor Built Environments. *Sustainability* **2019**, *11*, 4166. [[CrossRef](#)]
24. Zhang, X.; Ren, Z.; Mei, F. *Heat Transfer Theory*; China Architecture and Building Press: Beijing, China, 2007.
25. Liu, J.; Heidarinejad, M.; Pitchurov, G.; Zhang, L.; Srebric, J. An extensive comparison of modified zero-equation, standard k- ϵ , and LES models in predicting urban airflow. *Sustain. Cities Soc.* **2018**, *40*, 28–43. [[CrossRef](#)]